

Research Article

Open Access



Sub-2 nm PtBi alloy nanoparticles on Bi-N-C single-atom catalyst for selective oxidation of glycerol to 1,3-dihydroxyacetone

Tongyu Tang¹, Hai Zhang¹, Hao-Fan Wang¹, Hongjuan Wang¹, Yonghai Cao¹, Lingyun Zhou², Hao Yu^{1*}

¹School of Chemistry and Chemical Engineering, Guangdong Provincial Key Lab of Green Chemical Product Technology, South China University of Technology, Guangzhou 510641, Guangdong, China.

²School of Chemical Engineering, Guizhou Minzu University, Guiyang 550025, Guizhou, China.

*Correspondence to: Prof. Hao Yu, School of Chemistry and Chemical Engineering, Guangdong Provincial Key Lab of Green Chemical Product Technology, South China University of Technology, 381 Wushan Road, Tianhe District, Guangzhou 510641, Guangdong, China. E-mail: yuhao@scut.edu.cn

How to cite this article: Tang, T.; Zhang, H.; Wang, H. F.; Wang, H.; Cao, Y.; Zhou, L.; Yu, H. Sub-2 nm PtBi alloy nanoparticles on Bi-N-C single-atom catalyst for selective oxidation of glycerol to 1,3-dihydroxyacetone. *Chem. Synth.* **2025**, *5*, 28. <https://dx.doi.org/10.20517/cs.2024.84>

Received: 3 Jul 2024 **First Decision:** 2 Aug 2024 **Revised:** 8 Sep 2024 **Accepted:** 20 Sep 2024 **Published:** 24 Feb 2025

Academic Editor: Jin Xie **Copy Editor:** Pei-Yun Wang **Production Editor:** Pei-Yun Wang

Abstract

Nanoscale metal particle-decorated single-atom catalysts (SACs) have been widely used in the fields of photocatalysis, electrocatalysis and thermal catalysis due to the combination of the advantages of nanoparticles and SACs. Herein, a strategy based on Pt-Bi atomic exchange is proposed for the formation of ultrafine (sub-2 nm) PtBi nanoclusters on single atomic Bi-N-C. The dynamic structural evolution between single atomic Bi-N-C on nitrogen-doped carbon nanosheets and Pt nanoclusters on the reconfiguration of stable PtBi alloy nanoparticles was demonstrated through a spherical aberration-corrected transmission electron microscope, X-ray absorption spectroscopy and density functional theory calculations. By our synthesis strategy, the Bi-N-C sites significantly improve the dispersion of PtBi alloy nanoparticles, resulting in a high turnover frequency of up to 224.4 h⁻¹ and the 1,3-dihydroxyacetone selectivity of 77.4%, 3.5 times higher than that of commercial 5Pt/C. On the other hand, the strong interaction between SAC and nanoparticles enhanced the catalytic stability by preventing leaching of Bi. It opens new avenues toward the rational design of high-performance nanoparticle-SACs, enabled by the in-depth understanding of the interaction between nanoparticles and SACs, which determines the structure of real active sites.

Keywords: NP-SACs, sub-2 nm PtBi alloy nanoparticles, Pt-Bi atomic exchange, glycerol oxidation, 1,3-dihydroxyacetone



© The Author(s) 2025. **Open Access** This article is licensed under a Creative Commons Attribution 4.0 International License (<https://creativecommons.org/licenses/by/4.0/>), which permits unrestricted use, sharing, adaptation, distribution and reproduction in any medium or format, for any purpose, even commercially, as long as you give appropriate credit to the original author(s) and the source, provide a link to the Creative Commons license, and indicate if changes were made.



INTRODUCTION

As a by-product of the biodiesel production process^[1], the high-value utilization of glycerol (less than €0.5 per kg) is essential to improve the yield and competitiveness of biodiesel. Glycerol selective oxidation can produce glyceraldehyde (GLYD), glyceric acid (GA), 1,3-dihydroxyacetone (DHA) and other products of C2 and C1^[2]. Among them, DHA (~€132 per kg) can be used as a pharmaceutical intermediate and cosmetic addition^[3], which has high economic value and market demand. Au^[4,5], Pt^[6,7], and Pd^[8,9] are commonly used as heterogeneous catalysts for glycerol oxidation. Additionally, other non-noble metal catalysts, coupled with glycerol oxidation and CO₂ electroreduction, promote the formation of C1 oxygenated products^[10]. Au catalysts usually require strong alkaline conditions to display high catalytic activity for glycerol conversion^[5,11]. Under base-free conditions, Pt has a high catalytic performance in the oxidation of glycerol to GA and GLYD^[12]. However, improving the DHA selectivity of Pt catalyst in base-free oxidation of glycerol is still a great challenge.

Kimura *et al.* have modified Pt catalysts with Pb, Te, Se, Bi and Sb as additives, and found that doping Bi on Pt/C catalyst could increase the yield of DHA from 4% to 20%^[13]. To date, the Bi-promoted catalysts have been regarded as one of the most effective ones for the selective oxidation of glycerol to produce DHA^[7,14,15]. Several theories have been proposed to explain the promotion effect of Bi on secondary hydroxyl oxidation of noble metal nanoparticles (NPs), including inhibition of excessive oxidation of noble metals^[9,13], and geometric blocking effect^[9,13,16]. Bi is usually introduced into the catalyst in the form of alloys^[17,18], NPs^[19], or oxides^[13,20]. Ning *et al.* synthesized Pt-Bi catalysts in situ by directly adding bismuth salt or bismuth oxide to the glycerol reaction solution^[16]. It was revealed that the strong chelation of the reaction product GA with Bi³⁺ promoted the leaching of Bi from Pt-Bi catalysts, thus leading to unsatisfactory stability. Xiao *et al.* used density functional theory (DFT) to study the mechanism of Pt-Bi active sites in detail, and further confirmed that bismuth, as an ad-atom adjacent to Pt, rather than located in the interior of Pt, is the necessary condition for promoting DHA formation^[21]. In order to reduce the coverage of Bi on Pt NPs, the adjacent Pt-Bi active sites are preferred.

Metal NPs modified single-atom catalysts (SACs), named NP-SACs^[22], combine the advantages of both to enhance catalytic performance through four pathways: (1) Synergistic enhancement. NPs may provide alternative active sites for the adsorption and activation of a substrate, which is difficult at the SA sites^[23]; (2) Tandem enhancement. SA sites alone are active only for some reactions, while NPs provide sites for others^[24]; (3) Reinforcing enhancement. NPs can help adjust the geometric and electronic structure of the SA sites to optimize substrate adsorption/activation, thereby improving catalytic performance^[25]; (4) Parallel enhancement. NPs catalyze one or more reactions that SA sites cannot catalyze, meeting the requirements of multifunctional catalysis. He *et al.* studied the effect of Me-N-C SACs (Me=Co, Fe, Ni)-wrapped carbon nanotubes as support of Pt NPs on the base-free oxidation of glycerol^[26]. Me-N-C not only enhanced the dispersion of Pt, but also promoted the activation of oxygen, which significantly increased the glycerol conversion and turnover frequency (TOF). However, the primary hydroxyl oxidation of glycerol was dominant, and the DHA selectivity was much lower than GLYD. Huang *et al.* used nitrogen-doped carbon to load Bi single atoms^[27]. After loading Pt NPs, the adjacent Pt-Bi active sites can be generated, showing good glycerol oxidation activity and DHA selectivity. They suggested that the cooperation of Pt NPs with the adjacent Bi-N-C sites on the support promotes the oxidation of the secondary hydroxyl group. However, it is unclear if the coordination of single-atomic Bi with nitrogen may suppress the leaching of Bi. In addition, it is still understudied whether the interaction between SAs and NPs reconfigures the active sites due to the high activity of SAs and NPs in the heteronuclear NP-SACs. Liu *et al.* observed that, when applying reduction potential, the isolated Cu atoms migrated from the vertex position of the Au NP to the stable (100) plane of the first atomic layer of Au^[28]. DFT calculations showed that surface atomic migration

significantly regulated the electronic structure of Au, thereby improving the catalytic performance. Therefore, exploring the dynamic surface structure evolution between SA and NPs at the atomic level is important to identify the real active site that determines the catalytic performance.

In this work, we focus on the interaction between single atomic Bi-N-C sites and Pt clusters, which may play a role in reconfiguration of catalytic active sites. A synthesis strategy of PtBi alloy nanoclusters was proposed based on surface atomic exchange between single atomic Bi-N-C sites on nitrogen-doped carbon nanosheets and Pt NPs by impregnation-reduction^[29,30]. It was uncovered that when reduced in H₂, the Pt clusters underwent an atomic exchange with Bi-N-C sites to form stable Pt-Bi alloy NPs driven by thermodynamics. Thanks to the kinetic barrier caused by the strong Bi-N bonding, homogeneous and ultrafine (sub-2 nm) PtBi alloy NPs were generated, offering maximally exposed Pt atoms and stable Pt-Bi adjacency. The catalytic performance in the glycerol oxidation reaction was systematically studied to demonstrate the improved DHA yield and catalyst stability.

EXPERIMENTAL

Materials

Bismuth powder (99.99%), bismuth nitrate pentahydrate (99%), melamine (99%), ammonium chloride (GR, 99.8%), Pt/C catalyst and chloroplatinic acid (ACS, Pt 37.5% min) are purchased from Aladdin. Glycerin (AR) and glucose (99%) are purchased from Sinopharm Chemical Reagent Co., LTD. DHA (99%), GLYD (90%) and potassium hydroxide (90%) are purchased from McLean. GA (20% aqueous solution) is purchased from TCI Reagent Co., LTD. All the reagents were used as received.

Preparation of Bi_xNC-*t*

A certain amount of bismuth powder, 5 g melamine, 1 g glucose and 5 g ammonium chloride were mixed by ball milling, and then the mixture was put into a tubular furnace. It was heated at 10 °C/min ramp to 550 °C and kept for one hour in Ar atmosphere, then heated at 5 °C/min ramp to *t* °C (*t* = 800 °C, 900 °C, 1,000 °C) and kept for two hours. After naturally cooled to room temperature, the resulting material was ground evenly and denoted as Bi_xNC-*t*. *x* refers to the amount [mg] of bismuth powder added.

Preparation of 5Pt/Bi_xNC-*t*(H₂)

First, 300 mg Bi_xNC-*t* and 300 mL deionized water were sonicated in a beaker for 20 min to obtain a homogeneous suspension. Then, 11 mL H₂PtCl₆ aqueous solution (1.45 mg/mL) was added dropwise to the suspension with stirring. After an additional 15 min sonication and continuous stirring for 30 min at room temperature, KOH aqueous solution (0.5 mol/L) was added to adjust pH to 9.5. The resulting homogeneous suspension was heated at 80 °C for 1.5 h. After filtering and drying in vacuum at 60 °C for 12 h, the solids were reduced in 40 vol.% H₂/Ar at 250 °C for 2 h. The Pt nominal loading was controlled at 5 wt.%. The catalyst is denoted as 5Pt/Bi_xNC-*t*(H₂).

Preparation of 2Bi-5Pt/NC-900(H₂)

First, 300 mg Bi₀NC-900, 11 mg Bi(NO₃)₃·5H₂O, and 300 mL deionized water were sonicated for 20 min to obtain a homogeneous suspension. Then, 11 mL H₂PtCl₆ aqueous solution (1.45 mg/mL) was added dropwise to the suspension with stirring. After an additional 15 min sonication and continuous stirring for 30 min at room temperature, KOH aqueous solution (0.5 mol/L) was added to adjust pH to 9.5. The resulting homogeneous suspension was heated at 80 °C for 1.5 h. After filtering and drying in vacuum at 60 °C for 12 h, the solids were reduced in 40 vol.% H₂/Ar at 250 °C for 2 h. Pt nominal loading is controlled at 5 wt.%. The catalyst is denoted as 2Bi-5Pt/NC-900(H₂).

Catalyst characterizations

The Pt and Bi contents in the catalysts were measured by an Agilent 5110 inductively coupled plasma emission spectrometer (ICP-OES). PANalytical X'Pert Powder diffractometer (XRD), equipped with a Cu K α radiation source ($\lambda = 0.15406$ nm), was used to analyze the phase of the catalysts within 5°~90° at a scanning speed of 2°/min. The textural structure was tested by N₂ physical adsorption-desorption at 77 K in a TriStarII3020 automatic specific surface area tester. The specific surface area was calculated by Brunauer-Emmett-Teller (BET) method. One HJY LabRAM Aramis laser confocal microscopic Raman spectrometer was used to characterize the defectiveness of carbon materials. X-ray photoelectron spectroscopy (XPS) was measured on a Thermo Scientific™ K-Alpha™TM spectrometer equipped with a monochromatic Al K α X-ray source (1,486.6 eV) at an operating power of 100 W. The measurements were conducted under vacuum ($P < 10^{-8}$ mbar). Binding energy correction was performed with reference to the C1s peak of 284.6 eV. The microscopical characterizations were carried out in a JEM-2100F (JEOL) field emission transmission electron microscope (TEM) and a Titan Themis 60-300 (FEI Company, USA) spherical aberration-corrected transmission electron microscope (AC-TEM). Combined with an XFlash 6TI60 (Bruker, Germany) X-ray energy dispersion spectrometer, the distribution of elements of the sample can be determined. The X-ray absorption spectroscopy was measured at BL14W1 station in the Shanghai Synchrotron Radiation Facility. The obtained XAS data was processed in Athena for background, pre-edge line and post-edge line calibrations.

The Pt dispersion of the catalysts was determined by CO stripping, conducted at room temperature in a cell connected to an electrochemical workstation (CHI 660D). A glass carbon electrode served as the working electrode, platinum wire acted as the counter electrode, and a Hg/Hg₂SO₄ electrode was used as the reference electrode. A volume of 10 μ L catalyst ink (2 mg/mL) was coated on the glass carbon electrode and dried. The electrochemical test was performed in a 0.5 mol/L H₂SO₄ solution.

Catalytic tests

The thermo-catalytic oxidation reaction of glycerol was carried out in a 25 mL three-neck flask with a reflux, a bubbler and a thermometer. An aqueous solution of glycerol (5 g, 10 wt.%) and 40 mg catalyst were added to the flask, which was then heated to 60 °C at 1,200 rpm. The reaction was initiated by passing a flow of oxygen (150 Ncm³/min) as the ultimate oxidant. After reaction, the oxygen flowmeter and heating device were immediately turned off and the flask was cooled in an ice-water bath to stop the reaction. The products in the reactor were then weighed. After filtration through a polyether sulfone filter head, the products were analyzed using an Agilent high-performance liquid chromatograph (HPLC 1260 Infinity), equipped with a Refractive Index Detector (RID), an ultraviolet (UV) detector and Bio-Rad Aminex HPX-87H Column. A 0.005 mol/L H₂SO₄ solution was used as the mobile phase. The detection conditions are as follows: the flow rate of the mobile phase is 0.5 mL/min, the column temperature is 65 °C, the wavelength of the UV detector is 210 nm, and the analysis time is 20 min. Quantitative analysis was carried out by external standard method.

Density functional theory calculation method

The periodic DFT executed in the Vienna ab initio simulation package (VASP 6) is applied for all the calculations^[31-34]. Exchange and correlation are treated within the Perdew-Burke-Ernzerhof (PBE) generalized gradient approximation (GGA)^[35]. The valence electrons are described by a plane wave basis set with the kinetic cutoff energy of 400 eV, and the core electrons are replaced by the projector augmented wave (PAW) pseudopotentials^[31,36]. To improve computational efficiency, a 3 \times 3 \times 1 Monkhorst-Pack k-point mesh is used for nitrogen-doped graphene, respectively. All the structures are calculated until the Hellman-Feynman forces on each ion are lower than 0.03 eV/Å. The optimized geometries of the nitrogen-doped graphene and Bi-modified nitrogen-doped graphene are shown in [Supplementary Figure 1](#).

The adsorption energy (ΔE) is calculated using

$$\Delta E = E_{\text{total}} - (E_{\text{slab}} + E_{\text{cluster}}) \quad (1)$$

in which E_{total} is the total energy of the whole system upon adsorption, E_{cluster} is the energy of the metal cluster, and E_{slab} is the energy of the nitrogen-doped graphene.

RESULTS AND DISCUSSION

DFT calculation for the PtBi alloy formation

DFT calculation was carried out to study the interaction between single atomic Bi-N₄ modified nitrogen-doped carbon nanosheets and Pt clusters. The binding energies of Pt and Bi atoms with a N₄ vacancy were compared. As shown in [Figure 1A](#) and [B](#), the binding energy of a Pt atom with N₄ is 2.6 times that of Bi, indicating that the formation of Pt-N₄ is preferred over Bi-N₄. The strong bonding was also observed for a Pt₄ cluster on the N₄ vacancy [[Figure 1C](#)]. It suggests that a reconfiguration may occur driven by thermodynamics when contacting Bi-N₄ SACs with Pt. To verify this, the adsorption of a Pt₄ cluster on Bi-N₄ was investigated^[27,30,37-39]. Four possible geometries of Pt₄/Bi₁N₄C_x were optimized and shown in [Figure 1D-G](#). As a Pt₄ cluster adsorbed on Bi₁N₄C_x, the four Bi-N bonds may be kept to form a supported Pt₄ cluster adjacent to Bi₁N₄C_x [[Figure 1D](#) and [E](#)], in which a Pt-Bi bond is generated. It agrees with the configuration proposed by Huang *et al.*^[27]. However, the stronger binding between Pt and N may facilitate the formation of Pt-N bonds [[Figure 1F](#) and [G](#)]. It is interesting that the Bi atom may be completely extracted from the Bi₁N₄ site to form an alloy cluster of Pt₄Bi₁ on a nitrogen-doped graphene sheet, in which four Pt-N bonds are formed [[Figure 1G](#)]. The binding energy of Pt₄Bi₁ alloy clusters is significantly higher than other configurations, indicating that Pt tends to alloy with Bi in Bi₁N₄ sites through the Pt-Bi atomic exchange when loading Pt on Bi₁N₄C_x SACs, rather than supported on Bi₁N₄C_x. Similar reconstruction has been observed when loading Pt NPs on Fe-N-C^[40] or Co-N-C^[41]. Since the formation of single Pt sites is thermodynamically favorable, the extraction of pre-loaded Fe or Co from the single atomic sites leads to the formation of Pt₃M alloys or intermetallic compounds, showing extraordinary stability and activity in the oxygen reduction reaction. Our DFT calculation suggests that the strategy could be employed for the synthesis of PtBi alloy NPs.

Formation of sub-2 nm PtBi NPs

The synthesis of PtBi alloy NPs on Bi-N-C is schematically shown in [Figure 2](#). Firstly, single atomic Bi-N-C-modified nitrogen-doped carbon nanosheets are prepared by a one-step pyrolysis. Glucose, melamine, ammonium chloride and bismuth powder are mixed evenly by ball milling and calcined under inert atmosphere. Among them, glucose and melamine are carbon and nitrogen sources, respectively. Ammonium chloride assists the transportation of metal by converting Bi to bismuth chloride, whose diffusion contributes to the capture of Bi at the defects of nitrogen-doped carbon nanosheets^[42]. After the impregnation of K₂PtCl₆, the reduction at 250 °C under H₂ atmosphere enables the atomic exchange between Pt and single atomic Bi-N-C to generate the PtBi alloy NPs. Thanks to the strong binding between NPs and the N-containing vacant defects, the agglomeration among NPs is greatly suppressed, allowing for the formation of highly dispersed PtBi NPs.

A series of nitrogen-doped carbon nanosheets with different Bi addition amounts were obtained by pyrolysis at 800, 900 and 1,000 °C [[Supplementary Table 1](#)]. With the same Bi dosage, the Bi content decreases with the increase of temperature because of the increasing bismuth chloride evaporation. The pyrolysis at 800 and 900 °C resulted in considerable Bi contents in the products, which are suitable for the further preparation of PtBi catalysts for glycerol oxidation. The Zeta potential measurements indicate that

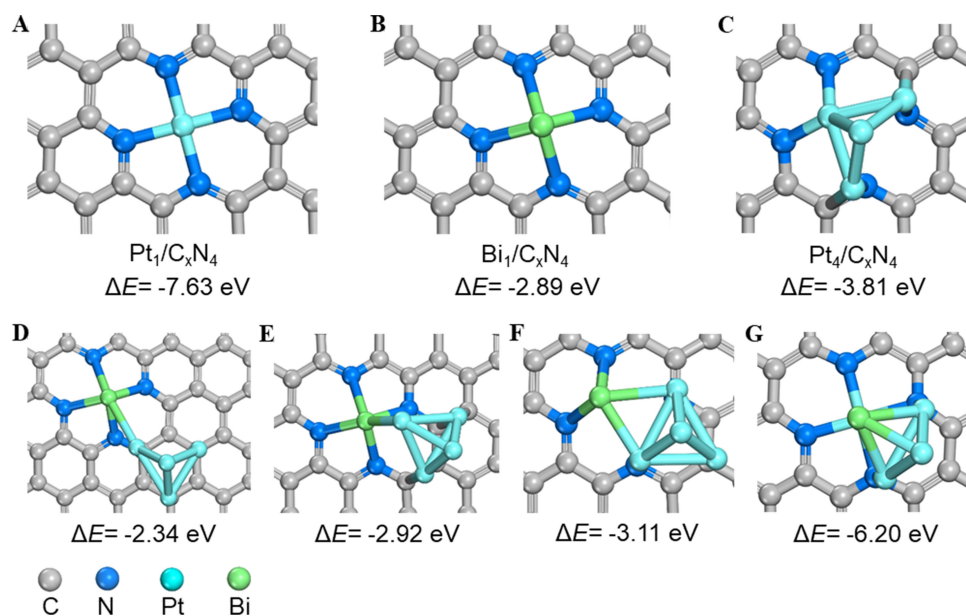


Figure 1. The optimized geometries and binding energies of (A) a single atomic Pt- N_4 site, (B) a single atomic Bi- N_4 site, and (C) a Pt_4 cluster on N_4 vacancy; (D-G) Four geometries and corresponding adsorption energies of a Pt_4 cluster on a single atomic Bi- N_4 site. The corresponding side views can be found in [Supplementary Figure 2](#).

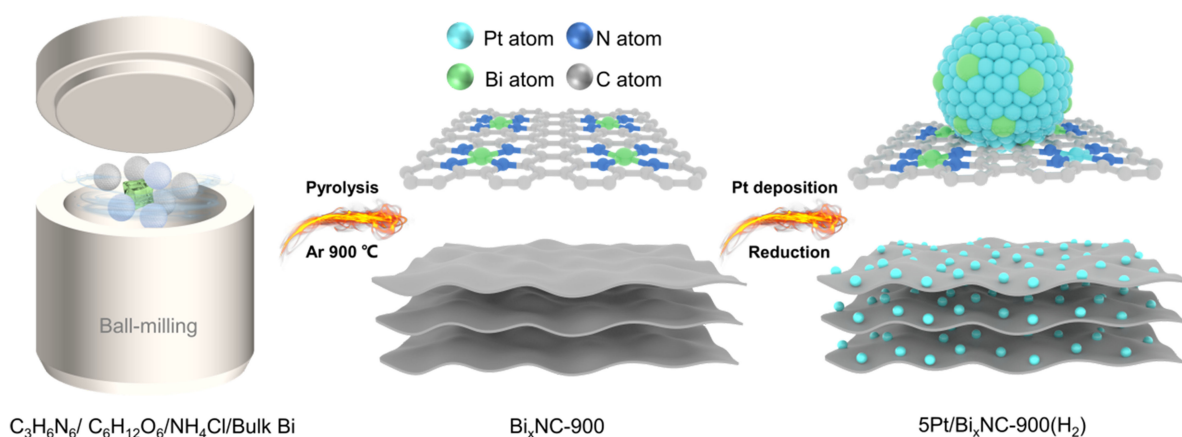


Figure 2. Schematic diagram of the synthesis of PtBi alloy nanoclusters on Bi-N-C.

the points of zero charge are dependent on the pyrolysis temperature [[Supplementary Figure 3](#)]. $Bi_xNC-800$ displays a point of zero charge between $pH = 4.5\sim 6.0$, while $Bi_xNC-900$ and $Bi_xNC-1000$ demonstrate this characteristic between $pH = 7.0\sim 8.5$. Since the subsequent deposition of Pt NPs requires a weakly alkaline condition for the adsorption of $PtCl_6^{2-}$, $900\text{ }^\circ\text{C}$ was selected as the optimal pyrolysis temperature for carbon nanosheet preparation. XRD analysis [[Supplementary Figure 4](#)] displayed that the condensed phases of Bi, such as Bi_2O_3 and Bi, are almost invisible in the XRD patterns of $Bi_xNC-900$ and $Bi_xNC-1000$, indicating the formation of highly dispersed/atomic Bi species. The N_2 adsorption-desorption measurements [[Supplementary Figure 5](#) and [Supplementary Table 2](#)] indicate that $Bi_xNC-900$ are mesoporous (about 5.5 nm) with a specific surface area of about $170\text{ m}^2/\text{g}$, facilitating the transportation and adsorption of glycerol molecules (about 0.5 nm in dynamics diameter)^[21]. The Raman spectra [[Supplementary Figure 6](#)] of $Bi_xNC-900$ show an intensity ratio I_D/I_G of ~ 1.00 , revealing the high defectiveness of carbon nanosheets.

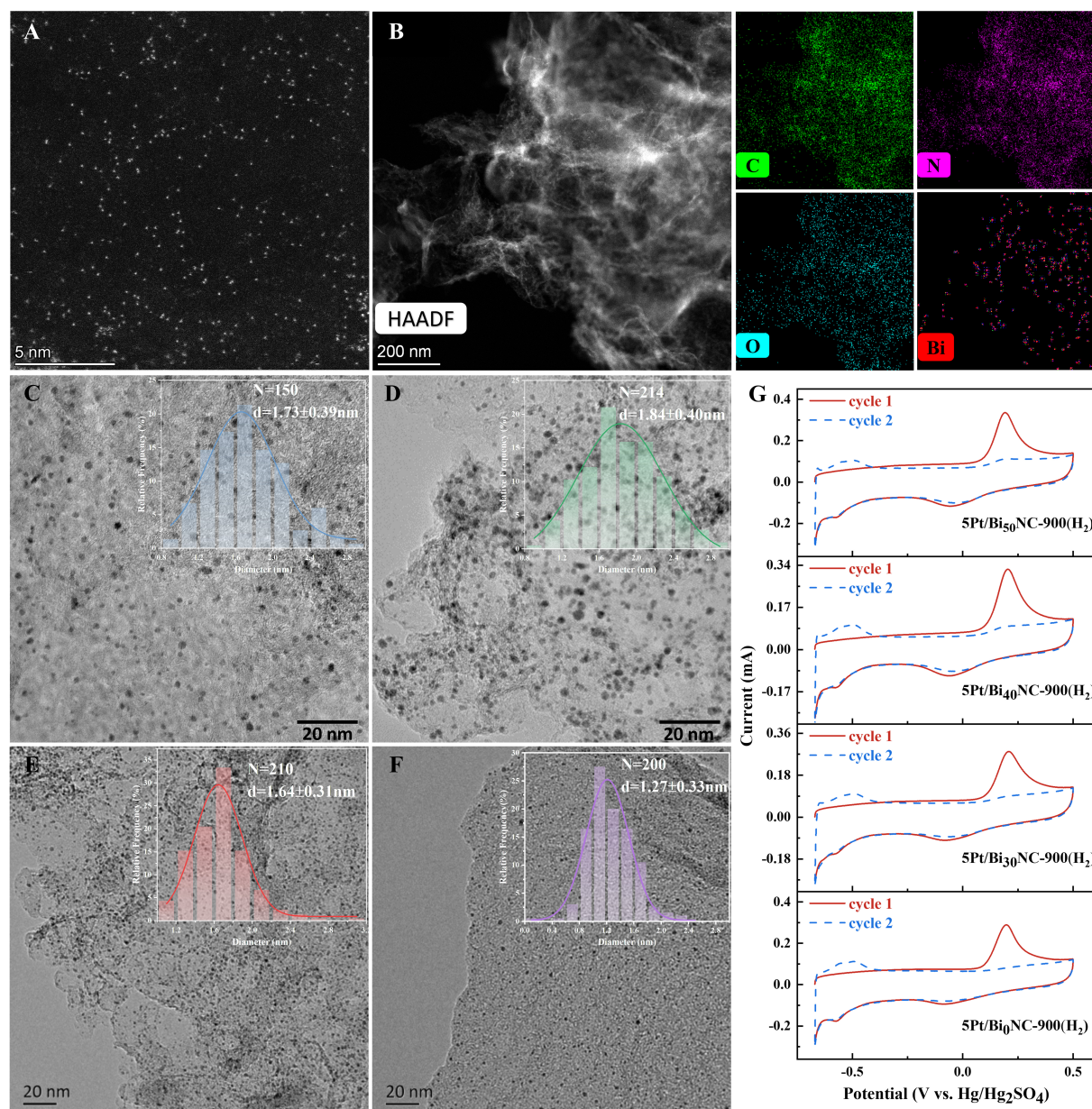


Figure 3. (A) AC-TEM image; (B) AC-HAADF-STEM image and corresponding EDS element maps of Bi₅₀NC-900; TEM images and histograms of NP diameters of (C) 5Pt/Bi₁₀NC-900(H₂), (D) 5Pt/Bi₃₀NC-900(H₂), (E) 5Pt/Bi₄₀NC-900(H₂), (F) 5Pt/Bi₅₀NC-900(H₂); (G) Cyclic voltammetry curves of CO electro-oxidation over 5Pt/Bi₅₀NC-900(H₂). AC-TEM: Aberration-corrected transmission electron microscope; AC-HAADF-STEM: aberration-corrected high-angle-annular-dark-field scanning transmission electron microscopy.

The TEM images of Bi_xNC-900 show the morphology of thin-layer carbon nanosheets, with the absence of metal NPs, which is consistent with the XRD result [Supplementary Figure 7]. A large number of uniformly dispersed Bi single atoms can be seen in AC-TEM images [Figure 3A], demonstrating the generation of Bi-N-C single sites. The high contrast image is recorded by aberration-corrected high-angle-annular-dark-field scanning transmission electron microscopy (AC-HAADF-STEM) due to the contribution of metal elements [Figure 3B]; meanwhile, it is observed that Bi is uniformly dispersed in the element distribution map. Using Bi_xNC-*t* as the support, Pt NPs with a nominal load of 5 wt.% were deposited by impregnation-reduction method with optimized conditions (impregnation pH of 9.5, H₂ reduction temperature at 250 °C

[Supplementary Figures 8 and 9]. 5Pt/Bi₃₀NC-800(H₂) shows a serious agglomeration of NPs, probably due to the inappropriate point of zero charge of Bi₃₀NC-800, as mentioned above [Supplementary Figure 10]. Pt NPs are uniformly distributed on Bi_xNC-900 [Figure 3C-F] with average particle diameters less than 2 nm, demonstrating the strong interaction of Bi-N-C single sites to anchor Pt NPs. The strong interaction with Bi-N-C single sites is further consolidated by the effect of Bi content in Bi_xNC-900. As shown in Table 1, with the increase of Bi content, the diameters of Pt NPs decreased from 1.8 to 1.3 nm on 5Pt/Bi₅₀NC-900(H₂). The Pt dispersion of 5Pt/Bi₅₀NC-900(H₂) measured by CO stripping reached 77.0%. However, the formation of Bi₂O₃ in Bi₆₀NC resulted in a large particle size. Similar trends are observed using the dispersion calculated by TEM observation^[26]. The above results confirmed that single atomic sites play a significant role in anchoring NPs^[43-46]. Song *et al.* have suggested that the anchoring effect of Co₁-N₄ sites and Pt strengthened the interaction between Pt and nanosheet support, thus significantly slowing down the aggregation of Pt NPs^[47]. The layered porous structure obtained by incorporating Fe into carbon support in the form of a single atom may limit the growth of intermetallic particle size of Pt₃Fe (about 2.5 nm)^[48]. To the best of our knowledge, it is the first report on the synthesis of such ultrafine sub-2 nm Pt NPs on carbon nanosheets assisted by the single atomic Bi-N-C sites.

The composition of supported ultrafine particles was further explored by AC-TEM. Figure 4A shows the STEM image of 5Pt/Bi₅₀NC-900(H₂) in the dark field. The energy-dispersive X-ray spectroscopy (EDS) line scanning of one of the uniformly distributed Pt NPs shows strong elemental signals of Pt and Bi [Figure 4B]. Furthermore, the EDS mapping indicates the high overlap of the appearance of Pt and Bi, suggesting the enrichment of Bi from single atomic Bi-N-C support around Pt NPs. The reconstruction of single atomic Bi-N-C was further ascertained by the microscopical analysis on AC-HAADF-STEM. As shown in Figure 4C-E, NPs on graphene sheets decorated by single atomic Bi-N-C are observed. The EDS mapping of the particulates clearly shows that the individual particles are composed of Pt and Bi, which proves the formation of PtBi alloy nanoclusters. The lattice spacings in Figure 4D and E display the Pt (111) and Pt (200) planes as highlighted. It should be noted that the measured spacings slightly deviate from the standard values of Pt (111) (0.227 nm) and Pt (200) (0.196 nm) planes, probably due to the alloying of Bi. Those results are consistent with the aforementioned DFT calculations; namely, the formation of PtBi alloy is thermodynamically favorable when Pt is deposited on single atomic Bi-N-C.

The chemical valences of Pt and Bi of Bi_xNC-900 and 5Pt/Bi_xNC-900(H₂) were analyzed by XPS. As shown in Figure 5A, the Bi 4f binding energy of Bi₅₀NC-900 is between those of elemental Bi (4f_{5/2}: 162.9 eV, 4f_{7/2}: 157.6 eV)^[18,49] and Bi₂O₃ (4f_{5/2}: 164.7 eV, 4f_{7/2}: 159.4 eV)^[50], indicating the valence of Bi single atoms of between 0 and +3^[51]. After loading Pt, in addition to the peaks of Bi single atoms, two peaks appear at 158.1 and 163.4 eV, slightly higher than the characteristic peaks of Bi(0), attributed to the formation of Pt-Bi bonds in the PtBi alloy. The Pt 4f XPS spectra are deconvoluted to Pt⁰, Pt²⁺ and Pt⁴⁺ [Figure 5B]^[52-55], with relative contents of 66.4%, 17.7%, 15.9% for 5Pt/Bi₀NC-900(H₂), and 59.7%, 29.2%, 11.1% for 5Pt/Bi₅₀NC-900(H₂), respectively. The Pt⁰ 4f_{5/2} and Pt⁰ 4f_{7/2} binding energies of 5Pt/Bi₅₀NC-900(H₂) are located at 75.2 and 71.9 eV, respectively, which have a negligible shift of 0.1 eV compared with the case in the absence of Bi in support [5Pt/Bi₀NC-900(H₂)], indicating the weak electronic interaction between Pt and Bi. It should be noted that the binding energy of Pt(0) of 5Pt/Bi₅₀NC-900(H₂) is considerably higher than that of elemental Pt (about 71.1 eV^[55]), which may originate from the size effect^[56,57] or the incomplete oxidation state of Pt caused by the high activity of Pt on the surface of ultrafine particles.

The electron structure and coordination environment of Pt and Bi in Bi₅₀NC-900 and 5Pt/Bi₅₀NC-900(H₂) were further analyzed by X-ray absorption near edge structure (XANES) and extended X-ray absorption fine structure (EXAFS). As shown in the Bi-L₃ XANES spectrum [Figure 5C], the near-side absorption

Table 1. Metal contents, BET specific surface areas, average particle sizes and dispersions of Pt NPs in 5Pt/Bi_xNC-900(H₂)

Catalysts	Bi ^a (wt.%)	Pt ^b (wt.%)	S _{BET} (m ² /g)	d _{TEM} (nm)	D _{TEM} ^c (%)	D _{CO} ^d (%)
5Pt/Bi ₀ NC-900(H ₂)	-	3.73	160.3	1.7 ± 0.4	65.4	69.1
5Pt/Bi ₃₀ NC-900(H ₂)	1.32	4.43	149.5	1.8 ± 0.4	61.5	59.5
5Pt/Bi ₄₀ NC-900(H ₂)	1.57	4.08	130.8	1.6 ± 0.3	69.0	75.4
5Pt/Bi ₅₀ NC-900(H ₂)	1.98	3.91	161.3	1.3 ± 0.3	89.1	77.0
5Pt/Bi ₆₀ NC-900(H ₂)	1.81	3.99	175.9	1.9 ± 0.3	58.9	54.3

^{a,b}Bi and Pt contents were determined by ICP-OES; ^cD_{TEM} (%) = 5.66/r, where r is the radius of Pt NP (Å); ^dD_{CO} (%) = $\frac{Q_{CO} \times A_{r_{Pt}}}{m_{cat} \times \omega_{Pt} \times N_A \times 2 \times q_e}$, where Q_{CO} is the electric quantity for CO oxidation, A_{r_{Pt}} is 195.078, q_e is 1.6 × 10⁻¹⁹, N_A stands for Avogadro's constant 6.02 × 10²³, m_{cat} is the mass of catalyst, and ω_{Pt} is the actual Pt loading determined by ICP-OES. The corresponding CV profiles are shown in Figure 3G. BET: Brunauer-Emmett-Teller; NPs: nanoparticles; TEM: transmission electron microscope; ICP-OES: inductively coupled plasma emission spectrometer; CV: cyclic voltammetry.

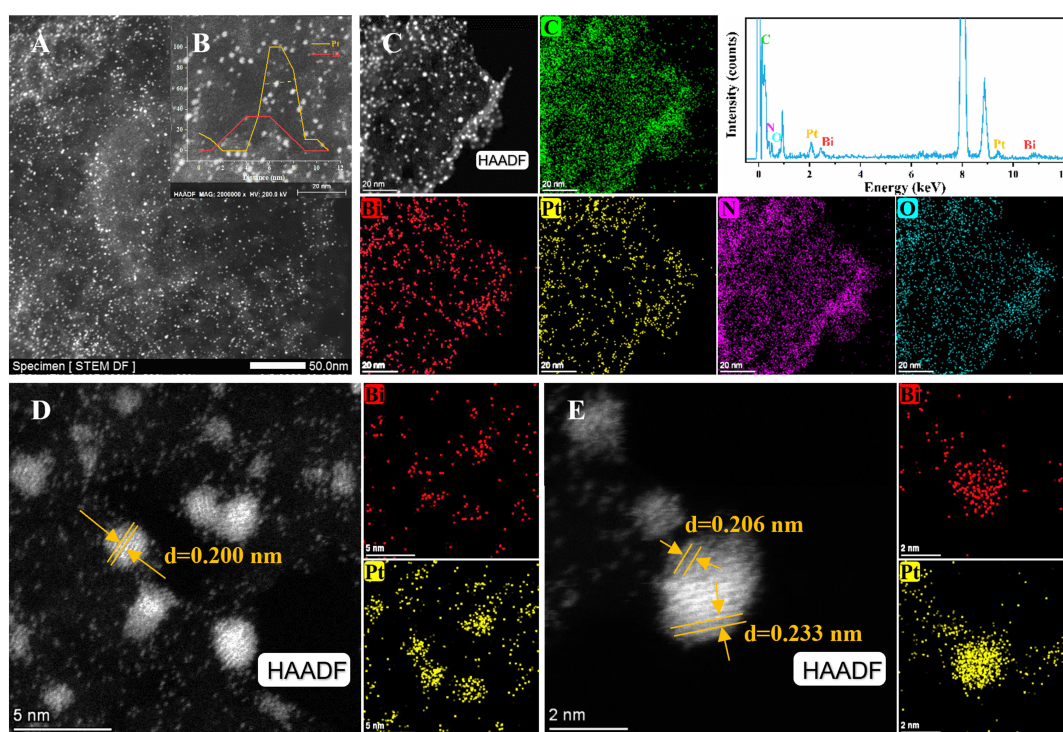


Figure 4. (A) STEM image; (B) EDS line scanning of a single particle; (C) AC-HAADF-STEM image and corresponding EDS spectrum and EDS element maps; (D-E) AC-HAADF-STEM image and EDS element maps of 5Pt/Bi₅₀NC-900(H₂). STEM: Scanning transmission electron microscopy; EDS: energy-dispersive X-ray spectroscopy; AC-HAADF-STEM: aberration-corrected high-angle-annular-dark-field scanning transmission electron microscopy.

energy and white line peak of Bi₅₀NC-900 are between Bi foil and Bi₂O₃, revealing its typical electronic structure as Bi (0 < δ < 3)^[50,51], which is consistent with the results of XPS. The R-space EXAFS spectra of Bi₅₀NC-900 and 5Pt/Bi₅₀NC-900(H₂) have obvious peak heights observed at 1.61 and 1.63 Å, respectively [Figure 5D], which are different from Bi–Bi and Bi–O bonds, and can be attributed to Bi–N coordination. The above results demonstrate that the isolated Bi–N–C sites are dispersed on Bi₅₀NC-900, which still exist after loading Pt. The near-side absorption energy and white line peak of Pt L₃-edge in 5Pt/Bi₅₀NC-900(H₂) are higher than those of Pt foil [Figure 5E], and the main peak of the EXAFS spectrum in R-space at 1.66 Å belongs to Pt–O/N bond [Figure 5F]^[58]. It is consistent with the XPS results revealing the incomplete

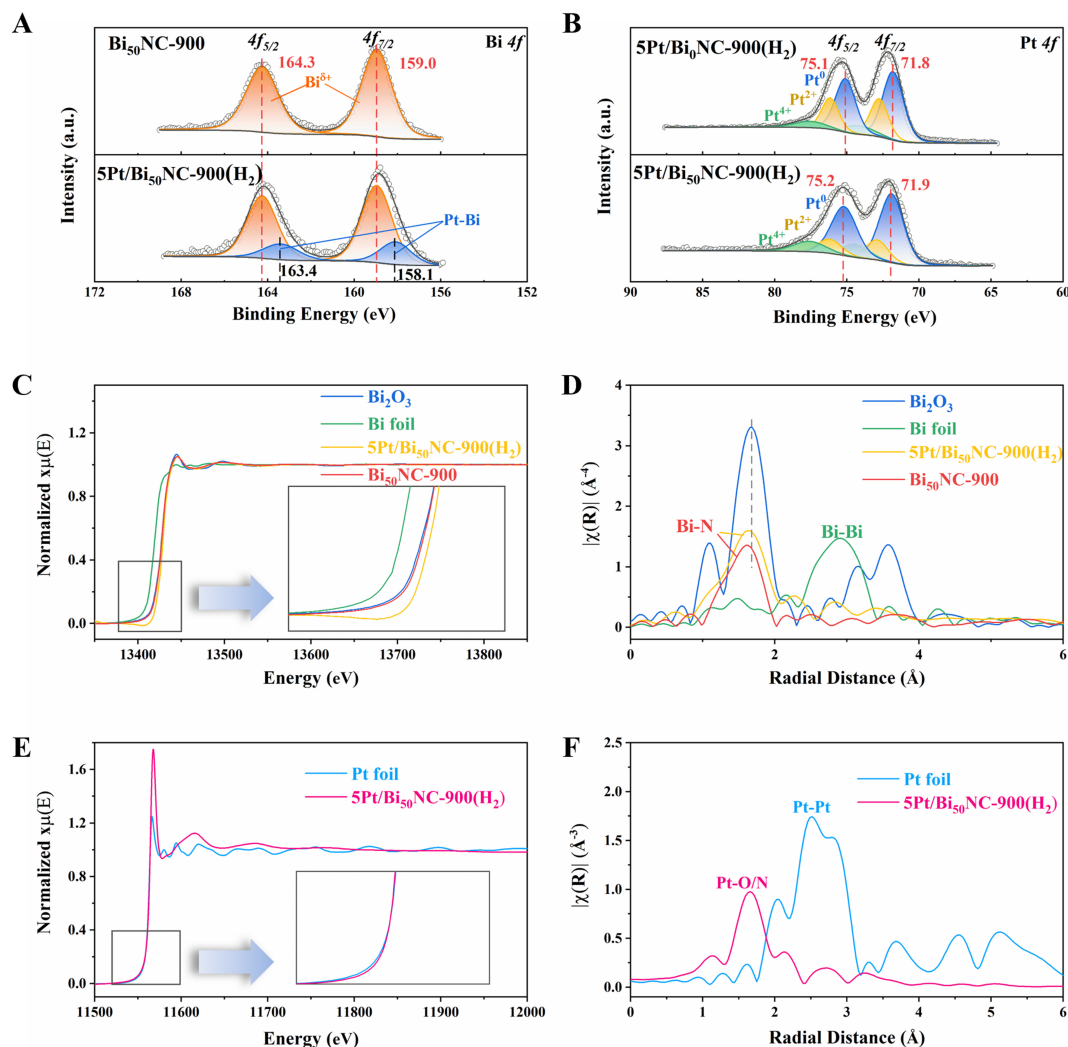


Figure 5. (A) Bi 4f XPS spectra of Bi₅₀NC-900 and 5Pt/Bi₅₀NC-900(H₂); (B) Pt 4f XPS spectra of 5Pt/Bi₀NC-900(H₂) and 5Pt/Bi₅₀NC-900(H₂); (C) Bi L₃-edge XANES; (D) Fourier-transformed EXAFS in the R-space of Bi; (E) Pt L₃-edge XANES; and (F) Fourier-transformed EXAFS in the R-space of Pt of Bi₅₀NC-900, 5Pt/Bi₅₀NC-900(H₂) and the reference sample. XPS: X-ray photoelectron spectroscopy; XANES: X-ray absorption near edge structure; EXAFS: extended X-ray absorption fine structure.

oxidation state of ultrasmall Pt particles, suggesting the high activity of surface Pt atoms.

Catalytic oxidation of glycerol

The synthesis temperature of Bi_xNC-*t* has a great impact on the activity of glycerol oxidation on 5Pt/Bi_xNC-*t*(H₂) [Supplementary Figure 11]. Notably, 5Pt/Bi_xNC-900(H₂) shows significantly higher activity and the DHA selectivity than the catalysts synthesized at 800 and 1,000 °C, indicating the importance of achieving highly dispersive PtBi NPs. It should be noted that the activity of 5Pt/Bi_xNC-900(H₂) is considerably higher than that of commercial 5Pt/C with a Pt NP diameter of about 3 nm [Supplementary Figure 11]. As shown in the time course in Figure 6A, all the 5Pt/Bi_xNC-900(H₂) catalysts display higher conversion of glycerol at 10 h even without Bi on support, indicating the high activity of ultrasmall Pt NPs (1.7 nm)^[7,59]. The highest pseudo-first-order reaction rate constant is achieved on 5Pt/Bi₄₀NC-900(H₂) and 5Pt/Bi₅₀NC-900(H₂), evidencing the importance of Bi incorporation with Pt NPs [Supplementary Figure 12]. The TOF of 5Pt/Bi₅₀NC-900(H₂) reaches 224.4 h⁻¹, which is superior to most of PtBi catalysts in literature

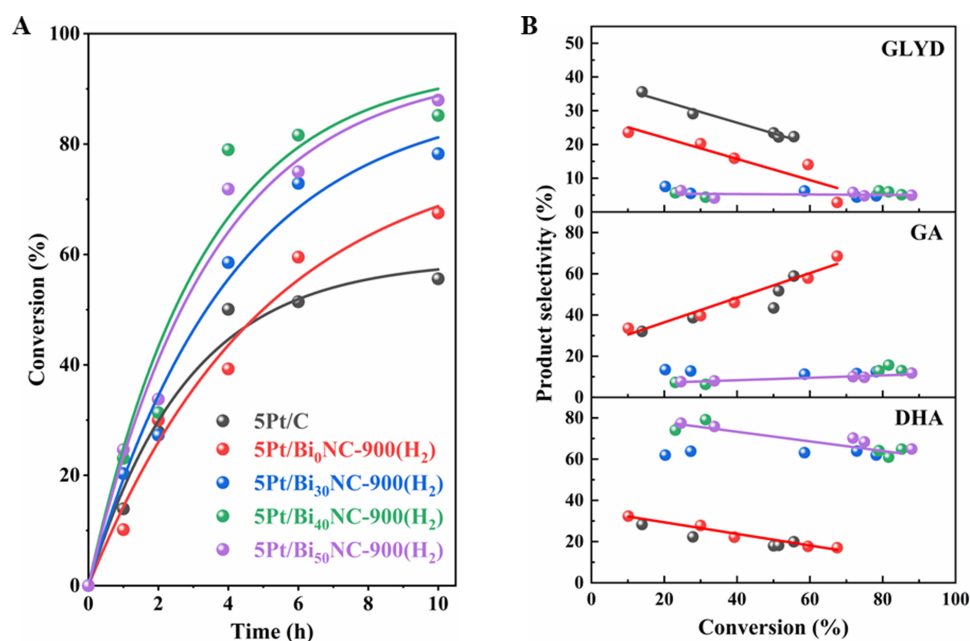


Figure 6. (A) Time courses and (B) selectivity-conversion relationships of glycerol oxidation over 5Pt/Bi_iNC-900(H₂) and commercial 5Pt/C catalysts. (Reaction conditions: 5 g 10 wt.% glycerol solution, 40 mg catalyst, glycerol/Pt molar ratio = 670, O₂ flow at 150 Ncm³/min, 1,200 rpm, 60 °C.)

[Supplementary Table 3].

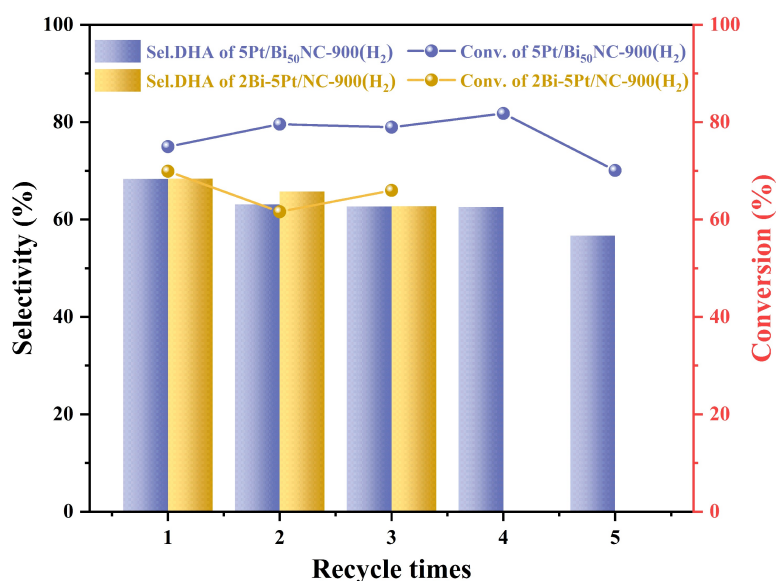
The incorporation of Bi significantly elevated the selectivity of DHA. As shown in Figure 6B, despite the higher activity of 5Pt/Bi_iNC-900(H₂) than commercial Pt/C, their dependences of DHA selectivity on glycerol conversion are similar. However, all the Bi-containing catalysts display high DHA selectivity at least three times and correspondingly reduced selectivity toward GLYD and GA. The DHA selectivity of 5Pt/Bi₅₀NC-900(H₂) reached 77.4% at 1h, and slightly descended with the progress of the reaction, possibly due to the adsorption of the by-product GA, which leads to partial coverage of the active area^[60,61]. At 60 °C for 10 h, the glycerol conversion of 5Pt/Bi₅₀NC-900(H₂) can reach 88.0% with a DHA selectivity of 64.9%. The above results confirm that the Bi-modified Pt catalyst could effectively promote the secondary hydroxyl oxidation of glycerol, and the intrinsic activity of Pt is also significantly enhanced.

To evaluate the stability, 5Pt/Bi₅₀NC-900(H₂) was reused for five cycles. After the reaction for 6h, the catalyst is filtered and separated from the reaction liquid, and then, the recovered catalyst is washed and dried in vacuum. To remove GA adsorbed on the catalyst surface^[60-62], the recovered catalyst was annealed at 250 °C in Ar atmosphere for 3h before the next glycerol oxidation reaction. As shown in Figure 7, in the second cycle reaction, the glycerol conversion increases by 4.6%, and the DHA selectivity decreases slightly by 5.0%. The glycerol conversion was almost unchanged after five cycles and a slight decrease of 4.8% was observed in the DHA selectivity, which may be due to the weak agglomeration of PtBi NPs caused by repeated annealing at 250 °C^[63,64]. The TEM observation demonstrates that the average particle size increased to 2.3 nm after the fourth annealing [Supplementary Figure 13]. The counterpart catalyst 2Bi-5Pt/NC-900(H₂) synthesized by co-reduction of Pt and Bi on Bi₀NC-900 carbon nanosheets showed a decrease of 8.3% in glycerol conversion at the second cycle reaction under the same reaction conditions. Meanwhile, the glycerol conversion of 2Bi-5Pt/NC-900(H₂) is significantly lower than that of 5Pt/Bi₅₀NC-900(H₂). This may be due to the uneven size distribution of 2Bi-5Pt/NC-900(H₂) metal NPs [Supplementary Figure 14]. The

Table 2. The composition, Pt dispersion of 5Pt/Bi₅₀NC-900(H₂) and 2Bi-5Pt/NC-900(H₂) and the contents of Bi in reaction liquid measured by ICP-OES

Catalysts	Bi ^a (wt.%)	Pt ^b (wt.%)	<i>d</i> _{TEM} (nm)	<i>D</i> _{TEM} ^c (%)	<i>D</i> _{CO} ^d (%)	Bi content in the reaction liquid after 6 h (mg/L)
5Pt/Bi ₅₀ NC-900(H ₂)	1.98	3.91	1.3 ± 0.3	89.1	77.0	0.0017
2Bi-5Pt/NC-900(H ₂)	2.28	3.53	2.0 ± 0.4	57.8	56.1	0.0359

^{a,b}Bi and Pt contents were determined by ICP-OES; ^c*D*_{TEM} (%) = 5.66/*r*, where *r* is the radius of Pt NP (Å); ^d*D*_{CO} (%) = $\frac{Q_{CO} \times A_{r_{Pt}}}{m_{cat.} \times \omega_{Pt} \times N_A \times 2 \times q_e}$, where *Q*_{CO} is the electric quantity for CO oxidation, *A*_{r_{Pt}} is 195.078, *q*_e is 1.6 × 10⁻¹⁹, *N*_A stands for Avogadro's constant 6.02 × 10²³, *m*_{cat.} is the mass of catalyst, and *ω*_{Pt} is the actual Pt loading determined by ICP-OES. ICP-OES: Inductively coupled plasma emission spectrometer; TEM: transmission electron microscope; NP: nanoparticle.

**Figure 7.** Recycling experiments of glycerol oxidation over 5Pt/Bi₅₀NC-900(H₂) and 2Bi-5Pt/NC-900(H₂). (Reaction conditions: 5 g 10 wt.% glycerol solution, 40 mg catalyst, glycerol/Pt molar ratio = 670, O₂ flow at 150 Ncm³/min, 1,200 rpm, 60 °C, 6 h.)

corresponding CO stripping experiment shows that the Pt dispersion is 56.1%, significantly lower than that of 5Pt/Bi₅₀NC-900(H₂). More importantly, the PtBi alloy catalyst prepared by the co-reduction strategy may suffer from serious leaching of Bi due to the chelation effect of Bi with oxidation products, as revealed by our previous work^[16]. The Bi content in the reaction liquid separated after the glycerol oxidation reaction for 6 h was detected by ICP-OES. It is 21 times higher in the case of 2Bi-5Pt/NC-900(H₂) than that of 5Pt/Bi₅₀NC-900(H₂) [Table 2]. According to the leaching experiment, 1.01 wt.% of Bi in 2Bi-5Pt/NC-900(H₂) was lost after reaction, while only 0.05 wt.% of Bi in 5Pt/Bi₅₀NC-900(H₂) lost. This result evidently indicates that the strong coordination between Bi and N and the thermodynamics driven formation of PtBi from Bi-N-C sites significantly improved the stability of 5Pt/Bi₅₀NC-900(H₂), which not only enhances the catalytic stability but also is conducive to the product quality by avoiding the metallic impurities. It confirms the power of the two-step synthesis strategy of in the production of ultrasmall sub-2 nm, high-performance and stable-single atomic catalyst supported ultrafine NPs.

CONCLUSIONS

We revealed the surface reconstruction phenomenon between single atomic Bi-N-C and Pt nanoclusters through spherical aberration transmission electron microscopy, X-ray absorption spectroscopy and DFT theoretical calculations. Pt-Bi atomic exchange can easily occur when the Bi-N-C single atomic sites interact

with Pt driven by thermodynamics due to the stronger binding between Pt and N. Therefore, the original adjacent Pt/Bi-N-C will be transformed into more stable Pt-Bi alloy NPs. At the same time, the kinetic barrier caused by the strong Bi-N bonding which is undestroyed during Pt-Bi atomic exchange is conducive to the uniform dispersion of PtBi alloy nanoclusters. Ultrafine (sub-2 nm) PtBi alloy nanoclusters significantly improve the secondary hydroxyl oxidation of glycerol with TOF of 224.4 h⁻¹ and 3.5 times higher DHA selectivity than commercial 5Pt/C. It should be noted that the strong interaction between PtBi alloy nanoclusters and Bi-N-C significantly suppresses the leaching of Bi, offering improved recyclability. By comparing with the counterpart catalyst synthesized by co-reduction of Pt and Bi on Bi₀NC-900 carbon nanosheets, it is confirmed that the two-step synthesis strategy plays an important role in the synthesis of ultrafine sub-2 nm, high-performance and stable NP-SACs.

DECLARATIONS

Authors' contributions

Writing - original draft, visualization, investigation, formal analysis, data curation: Tang, T.

Methodology, visualization, validation: Zhang, H.

Writing - review and editing, supervision: Wang, H. F.; Wang, H.; Cao, Y.

Software, visualization, data curation, funding acquisition: Zhou, L.

Conceptualization, writing - review and editing, supervision, resources, funding acquisition: Yu, H.

Availability of data and materials

The data can be found in the [Supplementary Materials](#). More details are available from the corresponding author upon reasonable request.

Financial support and sponsorship

This work was supported by the National Natural Science Foundation of China (Nos. 22272056, 22078106, 22202048), Natural Science Foundation of Guangdong Province (2024B1515040016), and Guizhou Provincial Science and Technology Plan Project Natural Science Key Project (ZK[2022] 028).

Conflicts of interest

All authors declared that there are no conflicts of interest.

Ethical approval and consent to participate

Not applicable.

Consent for publication

Not applicable.

Copyright

© The Author(s) 2025.

REFERENCES

1. Gallezot, P. Process options for converting renewable feedstocks to bioproducts. *Green. Chem.* **2007**, *9*, 295. [DOI](#)
2. He, Z.; Ning, X.; Yang, G.; et al. Selective oxidation of glycerol over supported noble metal catalysts. *Catal. Today.* **2021**, *365*, 162-71. [DOI](#)
3. Walgode, P. M.; Faria, R. P. V.; Rodrigues, A. E. A review of aerobic glycerol oxidation processes using heterogeneous catalysts: a sustainable pathway for the production of dihydroxyacetone. *Catal. Rev.* **2021**, *63*, 422-511. [DOI](#)
4. Zope, B. N.; Hibbitts, D. D.; Neurock, M.; Davis, R. J. Reactivity of the gold/water interface during selective oxidation catalysis. *Science* **2010**, *330*, 74-8. [DOI](#) [PubMed](#)
5. Demirel-gülen, S.; Lucas, M.; Claus, P. Liquid phase oxidation of glycerol over carbon supported gold catalysts. *Catal. Today.* **2005**, *102-103*, 166-72. [DOI](#)

6. Garcia, A. C.; Kolb, M. J.; van, N. S. C.; et al. Strong impact of platinum surface structure on primary and secondary alcohol oxidation during electro-oxidation of glycerol. *ACS Catal.* **2016**, *6*, 4491-500. DOI
7. Liang, D.; Gao, J.; Wang, J.; Chen, P.; Hou, Z.; Zheng, X. Selective oxidation of glycerol in a base-free aqueous solution over different sized Pt catalysts. *Catal. Commun.* **2009**, *10*, 1586-90. DOI
8. Ribeiro, L. S.; Rodrigues, E. G.; Delgado, J. J.; Chen, X.; Pereira, M. F. R.; Órfão, J. J. M. Pd, Pt, and Pt-Cu catalysts supported on carbon nanotube (CNT) for the selective oxidation of glycerol in alkaline and base-free conditions. *Ind. Eng. Chem. Res.* **2016**, *55*, 8548-56. DOI
9. Mondelli, C.; Ferri, D.; Grunwaldt, J.; et al. Combined liquid-phase ATR-IR and XAS study of the Bi-promotion in the aerobic oxidation of benzyl alcohol over Pd/Al₂O₃. *J. Catal.* **2007**, *252*, 77-87. DOI
10. Fernández-caso, K.; Molera, M.; Andreu, T.; et al. Coupling glycerol oxidation reaction using Ni-Co foam anodes to CO₂ electroreduction in gas-phase for continuous co-valorization. *Chem. Eng. J.* **2024**, *480*, 147908. DOI
11. Purushothaman, R. K. P.; van, H. J.; van, E. D.; Melián-cabrera, I.; Meeldijk, J.; Heeres, H. An efficient one pot conversion of glycerol to lactic acid using bimetallic gold-platinum catalysts on a nanocrystalline CeO₂ support. *Appl. Catal. B. Environ.* **2014**, *147*, 92-100. DOI
12. Roz A, Fongarland P, Dumeignil F, Capron M. Glycerol to glyceraldehyde oxidation reaction over pt-based catalysts under base-free conditions. *Front. Chem.* **2019**, *7*, 156. DOI PubMed PMC
13. Kimura, H.; Tsuto, K.; Wakisaka, T.; Kazumi, Y.; Inaya, Y. Selective oxidation of glycerol on a platinum-bismuth catalyst. *Appl. Catal. A. Gen.* **1993**, *96*, 217-28. DOI
14. Garcia, R.; Besson, M.; Gallezot, P. Chemoselective catalytic oxidation of glycerol with air on platinum metals. *Appl. Catal. A. Gen.* **1995**, *127*, 165-76. DOI
15. Hu, W.; Knight, D.; Lowry, B.; Varma, A. Selective oxidation of glycerol to dihydroxyacetone over Pt-Bi/C catalyst: optimization of catalyst and reaction conditions. *Ind. Eng. Chem. Res.* **2010**, *49*, 10876-82. DOI
16. Ning, X.; Li, Y.; Yu, H.; Peng, F.; Wang, H.; Yang, Y. Promoting role of bismuth and antimony on Pt catalysts for the selective oxidation of glycerol to dihydroxyacetone. *J. Catal.* **2016**, *335*, 95-104. DOI
17. Zhang, B.; Jiang, Y.; Ren, J.; Qu, X.; Xu, G.; Sun, S. PtBi intermetallic and PtBi intermetallic with the Bi-rich surface supported on porous graphitic carbon towards HCOOH electro-oxidation. *Electrochim. Acta.* **2015**, *162*, 254-62. DOI
18. Feng, Y.; Shao, Q.; Lv, F.; et al. Intermetallic PtBi Nanoplates boost oxygen reduction catalysis with superior tolerance over chemical fuels. *Adv. Sci.* **2020**, *7*, 1800178. DOI
19. Xue, W.; Wang, Z.; Liang, Y.; Xu, H.; Liu, L.; Dong, J. Promoting role of bismuth on hydrotalcite-supported platinum catalysts in aqueous phase oxidation of glycerol to dihydroxyacetone. *Catalysts* **2018**, *8*, 20. DOI
20. Nie, R.; Liang, D.; Shen, L.; Gao, J.; Chen, P.; Hou, Z. Selective oxidation of glycerol with oxygen in base-free solution over MWCNTs supported PtSb alloy nanoparticles. *Appl. Catal. B. Environ.* **2012**, *127*, 212-20. DOI
21. Xiao, Y.; Greeley, J.; Varma, A.; Zhao, Z.; Xiao, G. An experimental and theoretical study of glycerol oxidation to 1,3-dihydroxyacetone over bimetallic Pt-Bi catalysts. *AIChE. J.* **2017**, *63*, 705-15. DOI
22. Chen, R.; Chen, S.; Wang, L.; Wang, D. Nanoscale metal particle modified single-atom catalyst: synthesis, characterization, and application. *Adv. Mater.* **2024**, *36*, e2304713. DOI PubMed
23. Kuai, L.; Chen, Z.; Liu, S.; et al. Titania supported synergistic palladium single atoms and nanoparticles for room temperature ketone and aldehydes hydrogenation. *Nat. Commun.* **2020**, *11*, 48. DOI PubMed PMC
24. Zhang, J.; Wang, M.; Gao, Z.; et al. Importance of species heterogeneity in supported metal catalysts. *J. Am. Chem. Soc.* **2022**, *144*, 5108-15. DOI
25. Yang, H.; Gao, S.; Rao, D.; Yan, X. Designing superior bifunctional electrocatalyst with high-purity pyrrole-type CoN₄ and adjacent metallic cobalt sites for rechargeable Zn-air batteries. *Energy. Storage. Mater.* **2022**, *46*, 553-62. DOI
26. He, Z.; Yang, G.; Wang, H.; Dai, F.; Peng, F.; Yu, H. Co-N-C-supported platinum catalyst: synergistic effect on the aerobic oxidation of glycerol. *ACS Sustainable Chem. Eng.* **2020**, *8*, 19062-71. DOI
27. Huang, N.; Zhang, Z.; Lu, Y.; et al. Assembly of platinum nanoparticles and single-atom bismuth for selective oxidation of glycerol. *J. Mater. Chem. A.* **2021**, *9*, 25576-84. DOI
28. Liu, X.; Ao, C.; Shen, X.; et al. Dynamic surface reconstruction of single-atom bimetallic alloy under operando electrochemical conditions. *Nano. Lett.* **2020**, *20*, 8319-25. DOI PubMed
29. Jia, L.; Bulushev, D. A.; Podyacheva, O. Y.; et al. Pt nanoclusters stabilized by N-doped carbon nanofibers for hydrogen production from formic acid. *J. Catal.* **2013**, *307*, 94-102. DOI
30. Ning, X.; Li, Y.; Dong, B.; et al. Electron transfer dependent catalysis of Pt on N-doped carbon nanotubes: effects of synthesis method on metal-support interaction. *J. Catal.* **2017**, *348*, 100-9. DOI
31. Kresse, G.; Hafner, J. Ab initio molecular dynamics for open-shell transition metals. *Phys. Rev. B. Condens. Matter.* **1993**, *48*, 13115-8. DOI PubMed
32. Kresse, G.; Furthmüller, J. Efficient iterative schemes for ab initio total-energy calculations using a plane-wave basis set. *Phys. Rev. B. Condens. Matter.* **1996**, *54*, 11169-86. DOI PubMed
33. Kresse, G.; Hafner, J. Ab initio molecular-dynamics simulation of the liquid-metal-amorphous-semiconductor transition in germanium. *Phys. Rev. B. Condens. Matter.* **1994**, *49*, 14251-69. DOI PubMed
34. Kresse, G.; Furthmüller, J. Efficiency of ab-initio total energy calculations for metals and semiconductors using a plane-wave basis set.

- Comput. Mater. Sci.* **1996**, *6*, 15-50. DOI
35. Kresse, G.; Hafner, J. Ab initio molecular dynamics for liquid metals. *Phys. Rev. B. Condens. Matter.* **1993**, *47*, 558-61. DOI PubMed
 36. Kresse, G.; Joubert, D. From ultrasoft pseudopotentials to the projector augmented-wave method. *Phys. Rev. B.* **1999**, *59*, 1758-75. DOI
 37. Sun, X.; Gao, X.; Chen, J.; et al. Ultrasmall Ru nanoparticles highly dispersed on sulfur-doped graphene for HER with high electrocatalytic performance. *ACS Appl. Mater. Interfaces.* **2020**, *12*, 48591-7. DOI
 38. He, Z.; Dong, B.; Wang, W.; et al. Elucidating interaction between palladium and N-doped carbon nanotubes: effect of electronic property on activity for nitrobenzene hydrogenation. *ACS Catal.* **2019**, *9*, 2893-901. DOI
 39. Wang, W.; Yang, G.; Wang, Q.; Cao, Y.; Wang, H.; Yu, H. Modifying carbon nanotubes supported palladium nanoparticles via regulating the electronic metal-carbon interaction for phenol hydrogenation. *Chem. Eng. J.* **2022**, *436*, 131758. DOI
 40. Ao, X.; Zhang, W.; Zhao, B.; et al. Atomically dispersed Fe-N-C decorated with Pt-alloy core-shell nanoparticles for improved activity and durability towards oxygen reduction. *Energy Environ. Sci.* **2020**, *13*, 3032-40. DOI
 41. Li, X.; He, Y.; Cheng, S.; et al. Atomic structure evolution of Pt-Co binary catalysts: single metal sites versus intermetallic nanocrystals. *Adv. Mater.* **2021**, *33*, e2106371. DOI PubMed
 42. Zhang, H.; Tang, T.; Wang, H.; Wang, H.; Cao, Y.; Yu, H. Topological conversion of nickel foams to monolithic single-atom catalysts. *Adv. Funct. Mater.* **2024**, *34*, 2312939. DOI
 43. Zhang, M.; Li, H.; Chen, J.; et al. A low-cost, durable bifunctional electrocatalyst containing atomic Co and Pt species for flow alkaline/acid hybrid fuel cell and Zn-Air battery. *Adv. Funct. Mater.* **2023**, *33*, 2303189. DOI
 44. Liang, L.; Jin, H.; Zhou, H.; et al. Cobalt single atom site isolated Pt nanoparticles for efficient ORR and HER in acid media. *Nano. Energy.* **2021**, *88*, 106221. DOI
 45. Gong, L.; Zhu, J.; Xia, F.; et al. Marriage of ultralow platinum and single-atom MnN₄ moiety for augmented ORR and HER catalysis. *ACS Catal.* **2023**, *13*, 4012-20. DOI
 46. Zeng, Y.; Liang, J.; Li, C.; et al. Regulating catalytic properties and thermal stability of Pt and PtCo intermetallic fuel-cell catalysts via strong coupling effects between single-metal site-rich carbon and Pt. *J. Am. Chem. Soc.* **2023**, *145*, 17643-55. DOI
 47. Song, Z.; Wang, X.; Wu, D.; Fu, X.; Zhang, L.; Luo, J. Nitrogen-coordinated cobalt single atoms for achieving Pt with superhigh power and stability in proton exchange membrane fuel cells. *ACS Sustainable Chem. Eng.* **2023**, *11*, 9804-15. DOI
 48. Zhao, T.; Li, Y.; Liu, J.; et al. Highly dispersed L₁₂-Pt₃Fe intermetallic particles supported on single atom Fe-N_x-C_y active sites for enhanced activity and durability towards oxygen reduction. *Chin. Chem. Lett.* **2023**, *34*, 107824. DOI
 49. Guan, J.; Yang, S.; Liu, T.; et al. Intermetallic FePt@PtBi core-shell nanoparticles for oxygen reduction electrocatalysis. *Angew. Chem. Int. Ed. Engl.* **2021**, *60*, 21899-904. DOI PubMed
 50. Wang, Z.; Wang, C.; Hu, Y.; et al. Simultaneous diffusion of cation and anion to access N, S co-coordinated Bi-sites for enhanced CO₂ electroreduction. *Nano. Res.* **2021**, *14*, 2790-6. DOI
 51. Zhang, E.; Wang, T.; Yu, K.; et al. Bismuth single atoms resulting from transformation of metal-organic frameworks and their use as electrocatalysts for CO₂ reduction. *J. Am. Chem. Soc.* **2019**, *141*, 16569-73. DOI
 52. Yue, B.; Ma, Y.; Tao, H.; et al. CN_x nanotubes as catalyst support to immobilize platinum nanoparticles for methanol oxidation. *J. Mater. Chem.* **2008**, *18*, 1747. DOI
 53. Chen, W.; Ji, J.; Duan, X.; et al. Unique reactivity in Pt/CNT catalyzed hydrolytic dehydrogenation of ammonia borane. *Chem. Commun.* **2014**, *50*, 2142-4. DOI
 54. Ning, X.; Yu, H.; Peng, F.; Wang, H. Pt nanoparticles interacting with graphitic nitrogen of N-doped carbon nanotubes: effect of electronic properties on activity for aerobic oxidation of glycerol and electro-oxidation of CO. *J. Catal.* **2015**, *325*, 136-44. DOI
 55. Moulder, J.; Stickle, W.; Sobol, W.; Bomben, K. D. Handbook of X-ray photoelectron spectroscopy. 1992. Available from: <https://www.semanticscholar.org/paper/Handbook-of-X-Ray-Photoelectron-Spectroscopy-Moulder-Stickle/6165d59e158c88267b1154c167da68bfca644f4a>. [Last accessed on 9 Oct 2024].
 56. Ge, S.; Fan, W.; Tang, X.; et al. Revealing the size effect of ceria nanocube-supported platinum nanoparticles in complete propane oxidation. *ACS Catal.* **2024**, *14*, 2532-44. DOI
 57. Tong, T.; Liu, X.; Guo, Y.; Norouzi, B. M.; Hu, Y.; Wang, Y. The critical role of CeO₂ crystal-plane in controlling Pt chemical states on the hydrogenolysis of furfuryl alcohol to 1,2-pentanediol. *J. Catal.* **2018**, *365*, 420-8. DOI
 58. Quan, L.; Chen, X.; Liu, J.; Fan, S.; Xia, B. Y.; You, B. Atomic Pt-N₄ sites in porous N-doped nanocarbons for enhanced on-site chlorination coupled with H₂ evolution in acidic water. *Adv. Funct. Mater.* **2023**, *33*, 2307643. DOI
 59. Lei, J.; Duan, X.; Qian, G.; Zhou, X.; Chen, D. Size effects of Pt nanoparticles supported on carbon nanotubes for selective oxidation of glycerol in a base-free condition. *Ind. Eng. Chem. Res.* **2014**, *53*, 16309-15. DOI
 60. Ning, X.; Zhan, L.; Wang, H.; Yu, H.; Peng, F. Deactivation and regeneration of *in situ* formed bismuth-promoted platinum catalyst for the selective oxidation of glycerol to dihydroxyacetone. *New. J. Chem.* **2018**, *42*, 18837-43. DOI
 61. Worz, N.; Brandner, A.; Claus, P. Platinum-bismuth-catalyzed oxidation of glycerol: kinetics and the origin of selective deactivation. *J. Phys. Chem. C.* **2010**, *114*, 1164-72. DOI
 62. Zhang, X.; Zhou, D.; Wang, X.; et al. Overcoming the deactivation of Pt/CNT by introducing CeO₂ for selective base-free glycerol-to-glyceric acid oxidation. *ACS Catal.* **2020**, *10*, 3832-7. DOI
 63. Yang, C. L.; Wang, L. N.; Yin, P.; et al. Sulfur-anchoring synthesis of platinum intermetallic nanoparticle catalysts for fuel cells. *Science* **2021**, *374*, 459-64. DOI

64. Zhang, J.; Ming, P.; Li, B.; Zhang, C. Ultralow platinum catalysts for high performance fuel cells: *in situ* encapsulation of platinum atoms and CoPt₃ in 3D hollow nanoshells. *J. Mater. Chem. A.* **2023**, *11*, 20488-96. DOI



Tongyu Tang

Tongyu Tang received her M.S. degree in Materials and Chemical Engineering from South China University of Technology under the supervision of Prof. Hao Yu in 2024. During master's studies, her research focused on preparation of highly dispersed Platinum-based alloy nanoparticles and their application in alcohol oxidation.



Hai Zhang

Hai Zhang obtained his bachelor's degree from Zhongyuan University of Technology in 2016 and his Ph.D. from South China University of Technology in 2024 under the supervision of Professor Hao Yu. He then joined Zhejiang University of Science and Technology as a lecturer. His current research interests focus on the application of carbon-based nanomaterials in electrocatalysis and electrical energy storage.



Hao-Fan Wang

Hao-Fan Wang received his B.E. and Ph.D. degrees from the Department of Chemical Engineering, Tsinghua University in 2013 and 2018, respectively. He then worked as a postdoctoral researcher at the AIST-Kyoto University Chemical Energy Materials Open Innovation Laboratory (ChEM-OIL) in Japan. In 2022, he joined the School of Chemistry and Chemical Engineering at South China University of Technology as an associate professor. His research focuses on the design, synthesis and regulation of precious-metal-free electrocatalysts for oxygen- and hydrogen-related energy conversion and storage systems.

**Hongjuan Wang**

Hongjuan Wang obtained her B. Sc. in Fine Chemical Engineering from Zhengzhou University of Light Industry in 1997 and her Ph.D. in Chemical Engineering from South China University of Technology under the supervision of Prof. Zhong Li in 2003. She then joined Prof. Feng Peng's group at South China University of Technology as an assistant research fellow. In 2010, she was promoted to associate professor at South China University of Technology. Her research interests include nanocatalytic materials and their application in energy electrocatalysis.

**Yonghai Cao**

Dr. Yonghai Cao received his B.E. degree from Xiangtan University in 2009 and his Ph.D. from South China University of Technology in 2014. He joined the School of Chemistry and Chemical Engineering at South China University of Technology in 2017. His main research interests focused on the synthesis and application of nanomaterials in the field of catalysis and environmental remediation.

**Lingyun Zhou**

Lingyun Zhou earned her Ph.D. in 2018 from the College of Chemistry and Chemical Engineering at Xiamen University, under the guidance of Professor Fu Gang. After completing a three-year postdoctoral position in Professor Fu's group, she joined the School of Chemical Engineering at Guizhou Minzu University in 2021. Her research primarily focuses on theoretical aspects of heterogeneous catalysis, employing density functional theory (DFT) to extract reasonable theoretical models from complex real-world catalytic systems and to uncover the relationship between catalyst structure and activity.



Hao Yu

Dr. Hao Yu is a professor of Chemical Engineering and the Vice Dean of the School of Chemistry and Chemical Engineering at South China University of Technology. He earned his Bachelor's, Master's and Ph.D. degrees in chemical engineering from the Department of Chemical Engineering at Tsinghua University. Dr. Yu's research interests are in novel catalysts based on low-dimensional carbon-based materials and their energy and environmental applications, catalysis and reaction engineering for sustainable chemical technologies.